Analysis of the internal structure of a carbonate damage zone: Implications for the mechanisms of fault breccia formation and fluid flow

Stefan Hausegger [a], Walter Kurz [b,*], Robert Rabitsch [a], Eva Kiechl [a], Franz-Josef Brosch [a]

[a] Institut für Angewandte Geowissenschaften, Technische Universität Graz, Rechbauerstr. 12, A-8010 Graz, Austria
[b] Institut für Erdwissenschaften, Universität Graz, Heinrichstr. 12, A-8010 Graz, Austria

ABSTRACT

A segment of the Salzach-Ennstal fault zone (Talhof fault, Eastern Alps) shows evidence for joint nucleation by layer-parallel shear, causing the formation of joint-bounded slices oriented at high angles (65–85°) with respect to the shear zone boundary (SZB). Subsequent slice rotation resulted in joint reactivation as antithetic shears, slice kinking, and breaking-up of the individual slices into smaller fragments. The latter process, due to the longitudinal constraint of slices with impeded shear zone widening, marked the transition to cataclasite formation and fault core evolution during shear localization. Cataclasites were subsequently cemented and underwent continuous shear deformation by re-fracturing. Cement precipitation from fluids therefore played a fundamental role in the evolution of the fault zone, with a cyclic change between an open and a closed permeability system during fault evolution. Stable isotope compositions ($\delta^{13}C$, $\delta^{18}O$) of fault rock cements indicate a continuous equilibration between protolith-derived fragments and cements precipitated from those fluids. This points to limited fluid amounts, only temporally replenished by meteoric water, and a hydraulic gradient that directed fluid flow from the damage zone towards the fault core.

© 2009 Elsevier Ltd. All rights reserved.

1. Introduction

Knowledge of the internal structure of brittle fault zones has been gathered from both field studies (e.g., Anderson, 1951; Tchalenko, 1970; Sibson, 1986; Chester and Logan, 1987; Chester et al., 1993; Caine et al., 1996; Billi et al., 2003a; Faulkner et al., 2003; Wibberley and Shimamoto, 2003), and laboratory experiments (e.g., Riedel, 1929; Reches, 1978; 1983; Logan et al., 1979, 1992; Reches and Dietrich, 1983; Chester and Logan, 1990; Sagy et al., 2001; Katz et al., 2003). Fluid infiltration into faults, and the subsequent fluid–rock interaction, influence the fault mechanical behaviour (Hubbert and Rubey, 1959; Janssen et al., 1998; Kurz et al., 2008). Characterization of the internal structure of fault zones is an essential pre-requisite to understanding and predicting their mechanical, hydraulic and seismic properties (e.g., Faulkner et al., 2003; Woodcock et al., 2007). Generally, the following structural elements may be discriminated across brittle fault zones (following

Chester and Logan, 1986; Caine et al., 1996; Caine and Foster, 1999; Billi et al., 2003a; Faulkner et al., 2003):

(1) The host rock, or protolith, consists of the rock mass bounding the fault-related structures.
(2) The damage zone is characterized by secondary faults of small displacement, veins, and networks of shear and extensional fractures generally related to the processes of fault growth. Generally, the transition from the host rock to the damage zone is quite gradual.
(3) The fault core is where shear displacement is localized. The core is associated with the development of fault rocks by bulk crushing, particle rotation, abrasion and grain size diminution that obliterate the original host rock fabric (e.g., Billi et al., 2003a,b; Storti et al., 2003; Billi and Storti, 2004; Billi, 2005, 2007).
(4) Following the definition of Vermilye and Scholz (1998), the process zone comprises those features that result directly from propagation of the fault tip. As the damage zone, the process zone is characterized by secondary faults of minor displacement, veins, and networks of shear and extensional fractures. It may overlap with the damage zone as well as with parts of the fault core.

* Corresponding author at: Institut für Erdwissenschaften, Universität Graz, Heinrichstr. 26, A-8010 Graz, Austria. Tel.: +43 316 380 5588; fax: +43 316 380 9870.
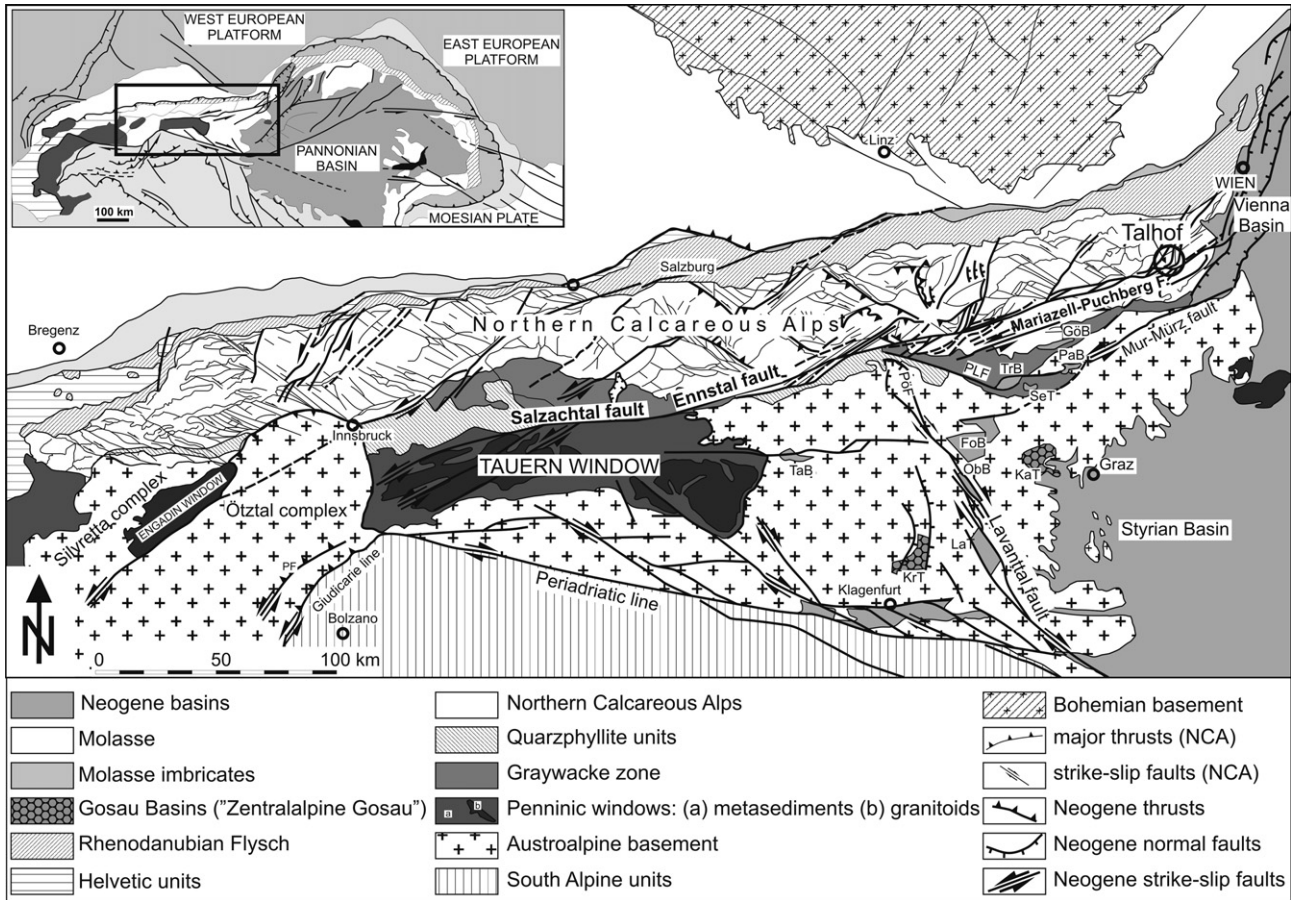E-mail address: walter.kurz@uni-graz.at (W. Kurz).

Fig. 1. Tectonic map of the Eastern Alps displaying the Palaeogene to Neogene fault system (after Linzer et al., 2002). The sites discussed in this contribution are located along the Talhof segment of the Salzach-Ennstal-Mariazell-Puchberg fault (SEMP) (see Fig. 2). *TH (encircled) = Talhof fault segment of the Salzach-Ennstal-Mariazell-Puchberg fault system*; AF = Ahrtal fault; AnF = Annaberg fault; BL = Brenner line; DHL: Döllach-Heiligenblut line; EL = Engadine line; GöF = Göstling fault; HoF = Hochstuhl fault; InF = Inntal fault; IsF = Iseltal fault; KL = Katschberg line; KLT = Königssee-Lammertal-Traunsee fault; LoF = Loisach fault; LS = Lower Schieferhülle; MöF = Mölltal fault; ÖT = Ötztal thrust; PF = Peijo fault; PeF = Pernitz fault; PLF = Palten-Liesing fault; PöF = Pöls fault; PyF = Pyhrn fault; RTS = Radstadt thrust system; RW = Rechnitz window; SaF = Salzsteig fault; TF = Telfs fault; WeF = Weyer fault; WGF = Windischgarsten fault; Z = Zell pull-apart structure; ZC = Zentralneiss core. GöT = Göriach basin; PaT = Parschlug basin; SeT = Seegraben basin; FoT = Fohnsdorf basin; ObT = Obdach basin; WiT Wiesenau basin; StT = St. Stefan basin.

The damage zone and the fault core may also be seen as representing the evolutionary steps of fault development. As the fault core evolves continuously within the damage zone (e.g., Billi et al., 2003a; Faulkner et al., 2003), the spatial zoning from the protolith to the core, including the development of fault rocks, corresponds to these evolutionary steps (e.g., Micarelli et al., 2006).

2. Objectives

In this study we discuss the structural evolution of carbonate fault rocks along a major fault zone in the Eastern Alps, and its implications for fluid flow and the permeability evolution within and along the fault zone. As fault zones highly affect the hydrogeological properties of the rock mass, we will discuss the role of fluids for fault zone evolution, and the interaction of these fluid phases with adjacent rocks. Information on these processes can be obtained from stable isotope compositions ($\delta^{13}C$, $\delta^{18}O$) of host rock fragments and cements that precipitated from fluids entrapped within the fault zone.

Structures that formed during the initial phases of fracturing, both along the fault segment described in this study and along other major faults in the Eastern Alps, were described in detail by Brosch and Kurz (2008). In this study we mainly focus on the

structures related to subsequent fault zone evolution. We focus mainly on the development of structures in the transition from the fault damage zone to the fault core up to the full development of fault rocks. The aim is to provide new insights into the structural
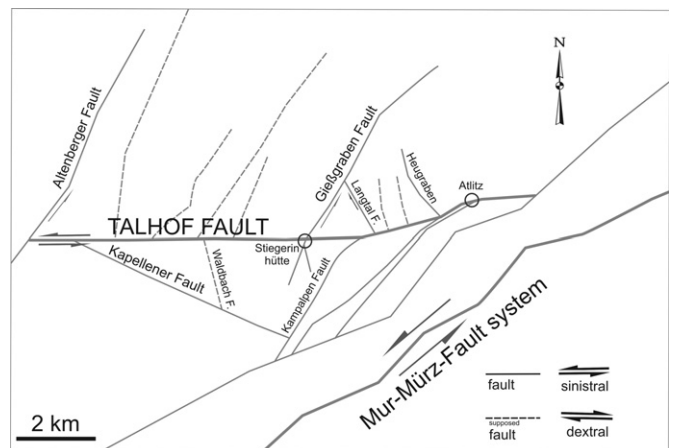

Fig. 2. Fault map showing the surface intersections and strike directions of the Talhof fault and associated conjugate faults (after Kiechl, 2007).

evolution of fault zones, the mechanisms of fault rock formation, and the related permeability evolution of fault zones.

In particular we present new observations on the internal structure of a major strike-slip fault within the Eastern Alps (Fig. 1). This structure is controlled by an anisotropic host rock fabric. The importance of fractures at high-angles to any pre-existing deformation-related anisotropy, being reactivated by layer-parallel shear, will be discussed in detail. The pre-existing anisotropy fabric, together with the repeated activation of discontinuities, has obliterated the original fracture-mechanical rock properties, and modified the angular relationships of fractures generated during faulting (e.g., Paterson, 1978; Rispoli, 1981; Peacock and Sanderson, 1992; Willemse et al., 1997; Mollema and Antonellini, 1999). Moreover, we focus on the role of these structures in the development of brittle shear zones and brecciation. Finally we investigate the fluid–rock interaction with emphasis on dissolution and precipitation mechanisms. Stable isotope analysis of selected samples provides information on the interaction of fractured domains and fault rocks with fluid phases and on the origin of fluids entrapped within the fault zone.

3. Methods of structural analysis

Samples were taken from the damage zone towards the fault core in order to infer the evolution of structures as displacement increases. Samples were saw-cut into serial sections parallel to the local direction of shear, and perpendicular to the shear zone boundary (SZB). The saw-cut sample sections were stained with black ink and subsequently polished in order to highlight the traces of the fracture network, voids and pores.

We describe the brittle structures by considering their orientation with respect to the shear direction along the shear zone boundary (SZB). Orientation distributions of distinct fracture sets were analysed by using the program package Tectonics FP 1.6.2, a 32-bit Windows™-Software for Structural Geology (Reiter and Acs, 1996–2001). The sizes of fragments and grains (maximum and
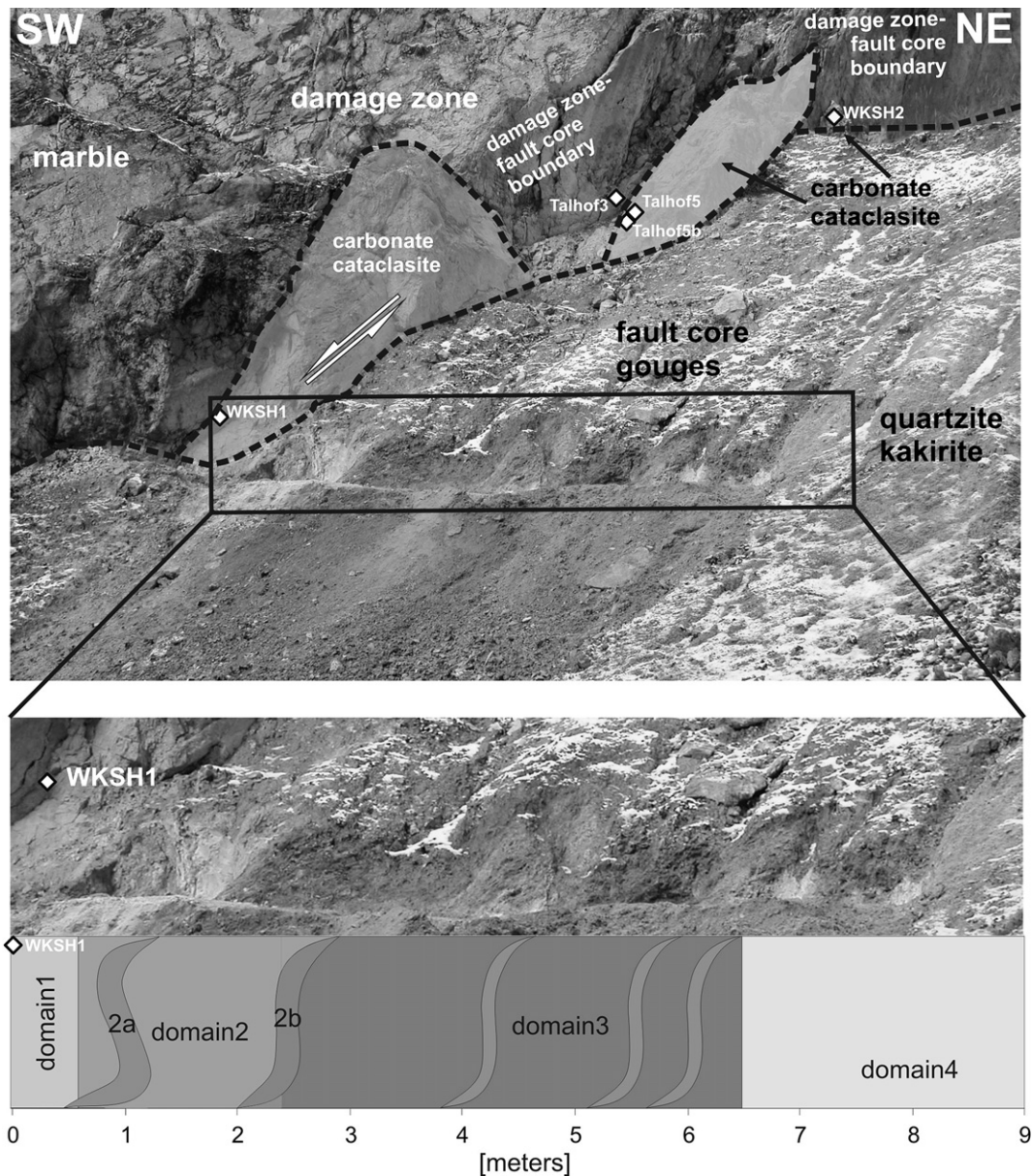

Fig. 3. Field view and section across the Talhof fault–Giessgraben fault intersection at site "Stiegerinhütte", including the subdivision of fault core domains (see text), and locations of sampling. For site coordinates see Appendix.

minimum diameter, F_{max} and F_{min}) were determined by measuring the normal distances between two tangents to the fragment margins at opposite points along the fragment boundaries, parallel to the longest and shortest fragment axes, respectively. This was done by the application of an automated image analysis package (analysis auto 5.0© 1986–2006, Olympus Soft Imaging Solution GmbH).

4. Geological and tectonic setting

We selected well exposed sites along the Talhof fault (Gmeindl, 1999), which is a 15 km long segment of the Salzach-Ennstal-Mariazell-Puchberg (SEMP) fault system in the Eastern Alps (Fig. 1) (Ratschbacher et al., 1989, 1991; Decker et al., 1993; Decker and Peresson, 1996; Wang and Neubauer, 1998; Frisch et al., 2000). The WSW–ENE oriented SEMP fault extends for 400 km along the Eastern Alps. The maximum left-lateral displacement along the SEMP is 70 km (Linzer et al., 2002). The fault trends sub-parallel to the regional orogenic strike from the western part of the Tauern Window to the Vienna Basin (Fig. 1), and crosses all Austroalpine tectono-stratigraphic units. The fault zone separates the Austroalpine and Penninic units of the central Eastern Alps, which experienced up to 50% of orogen-parallel extension during the Oligocene and Miocene (Frisch et al., 2000). The SEMP forms the lateral ramp of west- and east-directed detachment faults that accounted for the tectonic exhumation of the Tauern metamorphic dome. Deeper ductile structures of the segment forming the northern margin of the Tauern Window were exhumed by the late Neogene uplift of the Tauern metamorphic dome. On the contrary the central and eastern segments show brittle deformation distributed over a broad segmented shear zone with a thickness of up to several hundred meters (Frisch et al., 2000; Linzer et al., 2002).

In the area described in this study, the SEMP runs along boundary between the Lower Austroalpine Semmering-Wechsel nappe system, in the south, and the Upper Austroalpine nappe system, comprising the Greywacke zone and the Northern Calcareous Alps, in the north. Several nappes comprise pre-Alpine basement rocks covered by Permian to Mesozoic cover sequences. Assembly of Austroalpine nappes took place during the Early Cretaceous. The Lower Austroalpine nappes and part of the Greywacke zone were subsequently affected by greenschist facies metamorphism during Late Cretaceous times (for summary, see Schmid et al., 2004; Schuster and Kurz, 2005). The main thrusts
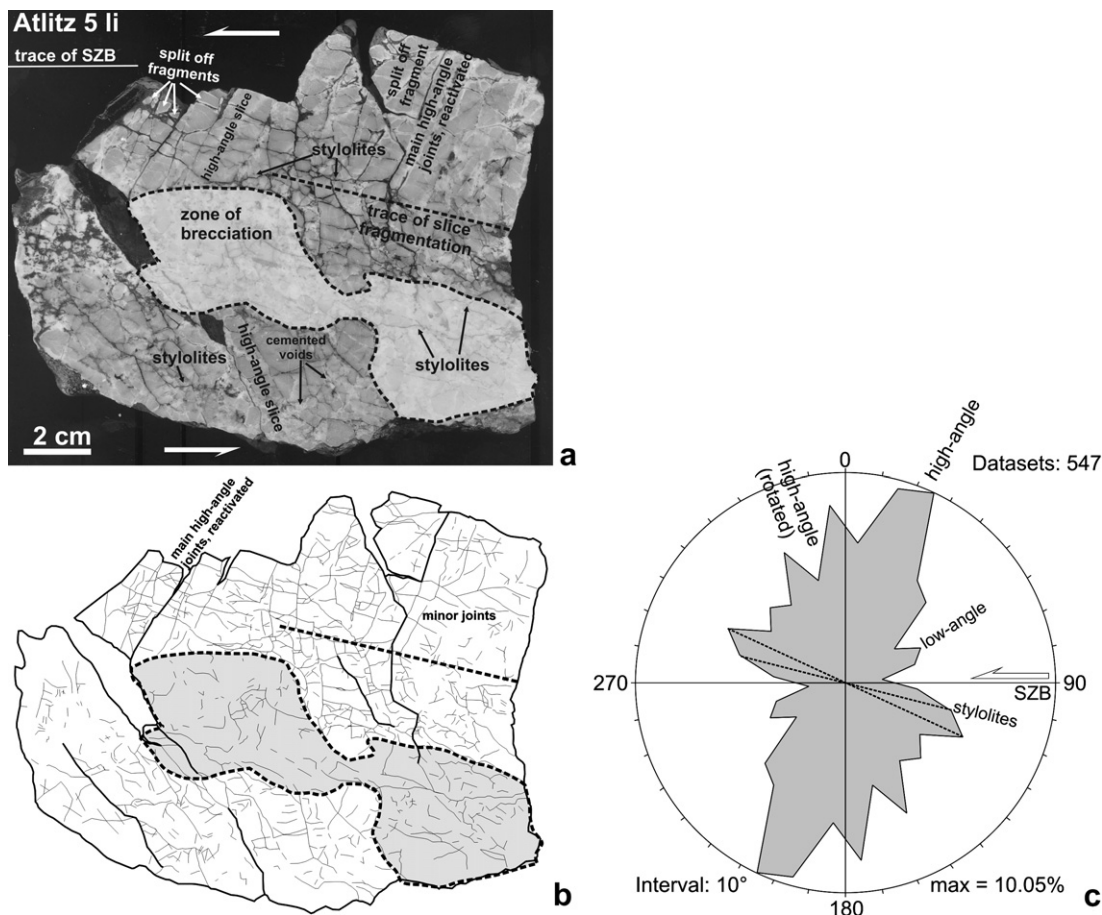

Fig. 4. (a), (b) Polished and stained sample sections showing the fracture pattern of carbonate rocks located within the Talhof fault damage zone, at a distance of approximately 60 cm from the damage zone–fault core contact. The shear zone boundary (SZB) runs parallel to the bedding/foliation. Slices with a thickness of approximately 1 cm are bordered by sub-vertical fractures (termed main fractures here) (thick lines) formed at high angles to the SZB. Slice-internal joints (termed minor fractures) (thin lines) either run sub-parallel to the SZB or occur as probably conjugate sets. Pressure solution seams (stylolites) form predominantly at low angles, 10–15° clockwise to the SZB. Slice-bounding fractures are partly dragged, the slices in the upper part of the samples are partly fractured and kinked, the trace of the fracture zone is marked by a stippled line. Slices in the lower part of the sample are rotated anticlockwise related to a sinistral sense of shear along the SZB. The fracture zone in the central part is characterized by the formation of slice-derived fragments embedded within a finer-grained carbonate matrix. The shear sense within the fracture zone coincides with the general sense of shear along the SZB. Sample from site "Atlitz" (see Appendix). (c) The Rose diagram displays the orientation of the distribution of slice-internal joints relative to the SZB, with a maximum frequency at 75–85° anticlockwise from the SZB, and additional maxima within the NW sector of the diagram, interpreted as rotated high-angle joints. Sub-maxima at low angles to the SZB are interpreted to represent conjugate minor shears to the SZB. Arrows indicate the displacement along reactivated structural elements.

and lithological boundaries, however, were reactivated and over-printed during Oligocene to Miocene strike-slip faulting. In the area of investigation, the Talhof fault mainly follows the boundary between Permian to Triassic quartzites and Anisian to Ladinian carbonates.

The subvertical, approximately E–W striking Talhof fault segment (Fig. 2) shows left-lateral displacement of approximately 2–3 km. It is cut by the NE-trending left-lateral Altenberg and Mur-Mürz faults in the west and in the east, respectively. The Talhof fault zone is morphologically marked by trenches and ridges formed by subvertical to steeply dipping carbonate beds.

5. Site description

The sites described in this study provide a nearly complete exposure of the Talhof fault segment, i.e. from the protolith to the fault core. Special emphasis will be given on a site exposing the intersection of the Talhof and Giessgraben fault zones (Fig. 3). At the Talhof–Giessgraben fault intersection (Fig. 2), Lower Triassic (Anisian) fine-grained layered marbles are separated from quartz-ites of Permian to Triassic protolith age, both belonging to the Lower Austro-Alpine unit (Fig. 1). Within the quartzites, the pro-tolith is almost totally disintegrated into loose, incoherent and incohesive cataclasites, up to the formation of clay-rich fault gouges with low cohesion (the fault core) (fault rock terminology after Brodie et al., 2002). Within the metamorphic carbonates, the fault-related deformation is concentrated along the nearly vertical discontinuities defined by a composite metamorphic foliation and sedimentary bedding that acted as slip planes. For this reason, the

latter are considered as the shear zone boundaries (SZB) (Brosch and Kurz, 2008). The general width of the fault zone is difficult to estimate due to the susceptibility of highly disintegrated parts to weathering and erosion. We measured a width ranging from a few meters to approximately 25 m.

The section exposed at the site "Stiegerinhütte" was subdivided into several structural domains, defined by the internal structure and the fabric of the fault rocks (Fig. 3). The damage zone adjacent to the core is made up of SW–NE striking layered carbonates showing a sharp, subvertical slickensided contact to the fault core. Domain 1 is characterized by cemented carbonate fault breccias and cataclasites with a thickness of up to 0.5 m. Domains 2–4 include fault rocks derived from a quartzitic protolith. Domain 2 has a thickness of approximately 1.5 m, and consists of fine-grained quartz-rich gouges (up to 90% quartz) with minor contents of carbonates. The grain size is usually less than 0.5 mm. Lenses of highly disintegrated basement gneisses, mainly transformed into fault gouges, are embedded in these fault gouges of domain 2. These lenses are displayed in sub-domains 2a and 2b (Fig. 3). Domain 3 is similar to domain 2 but is characterized by a larger grain size (0.7–2 mm) and by the lack of carbonates. Domain 4 consists of irregularly fragmented and un-cemented quartzite. Fragment sizes vary between 1 and 5 cm.

6. Evolution of joints and shear fractures at the damage zone–fault core transition

Rocks of the damage zone adjacent to domain 1 are character-ized by fractures at high (50–120°) and low (10–30°) angles
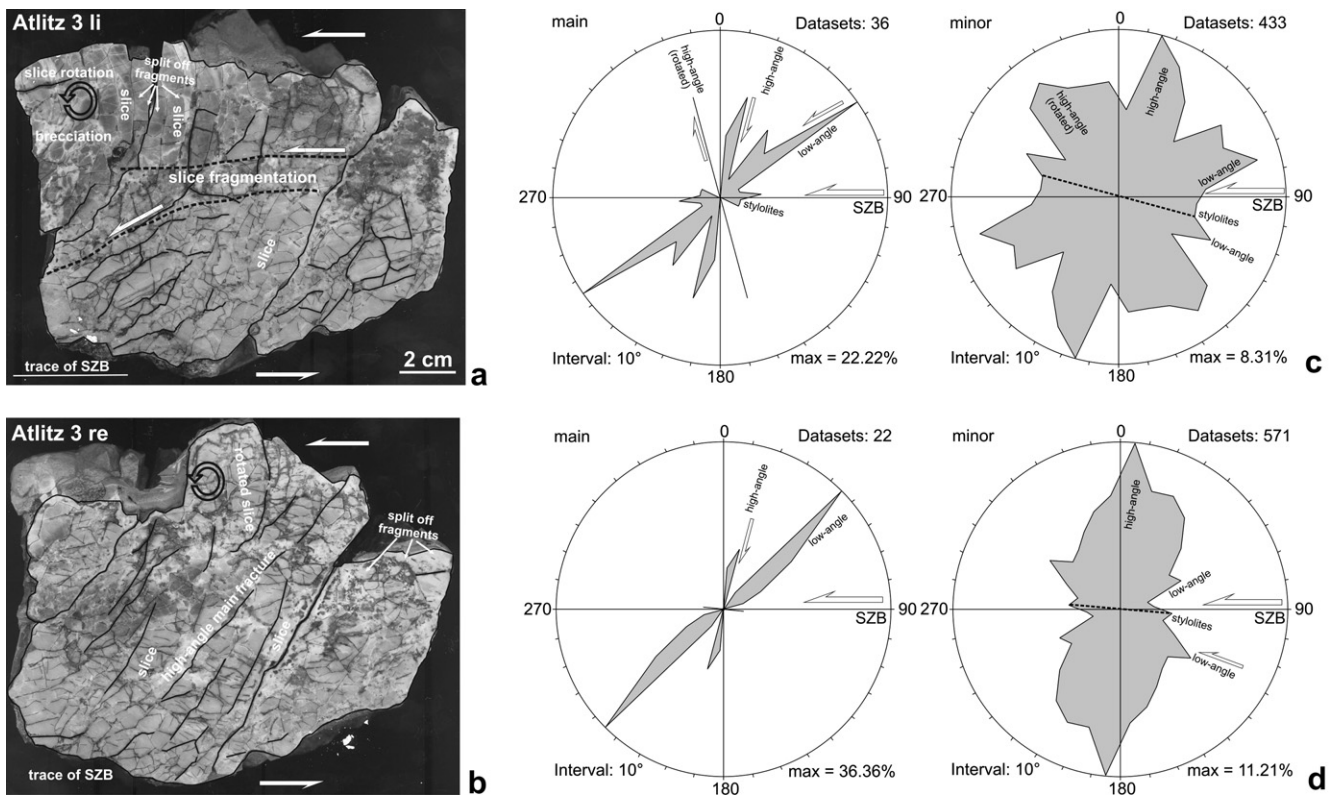

Fig. 5. (a), (b) Polished and stained sample sections showing the fracture pattern of carbonate rocks located within the Talhof fault damage zone at a distance of approximately 45 cm and 40 cm to the damage zone–fault core contact, respectively. Thick lines: main fractures, thin lines: minor joints. (c), (d) The Rose diagrams display the orientation of the distribution of slab-bounding (main) and slab-internal (minor) fractures relative to the shear zone boundary (SZB). Maximum frequencies of slice-bounding joints are located between 65° and 85° anticlockwise from the SZB, with additional maxima between 100° and 130° anticlockwise from the SZB. These are interpreted to represent rotated high-angle joints. Stylolites predominantly form at low angles, 10–15° clockwise to the SZB. Arrows indicate the displacement along reactivated structural elements. Sample from site "Atlitz" (see Appendix).

anticlockwise from to the shear zone boundary. In this study, these fractures are named as high- and low-angle fractures, respectively. The relative timing of fracture formation can be determined by abutting and crosscutting relationships.

Low-angle fractures at angles between 20 and 30°, measured in an anticlockwise sense to the SZB, are sheared fractures. Structures at angles between 0 and 20°, clockwise to the SZB, mostly are pressure solution seams (stylolites) (Figs. 4–9), and secondary shear fractures.

The high-angle fractures generally form within the moderately wide spaced layers, and mostly show subsequent reactivation as sheared fractures. This reactivation is indicated by the offset of the bedding and pre-existing foliation. Because of the subsequent reactivation, the mechanism of original fracture formation cannot be clearly determined. However, the lack of shear displacement in distinct domains suggests their formation as cross-joints (Mollema and Antonellini, 1999). Moreover, it cannot be excluded, that additional fractures formed as antithetic shears at high angles to

the SZB. This results in a general fabric dominated by a set of sub-parallel sheared joints and shear fractures at high angles (50–85°) anticlockwise from SZB (Figs. 4–6), with a spacing of 0.5–2 cm, and the evolution of a fracture cleavage, crosscutting the primary composite foliation. A frequency maximum of sheared fractures is developed at 75° (Fig. 4c). Consequently, the general structure is characterized as an array of roughly prismatic rock slices (Figs. 4a, b, 5a, b, 6a). These slices were termed "lamellae" by Brosch and Kurz (2008). The mean thickness of the slices in population varies between 2 and 25 mm, with mean values between 7.5 and 20 mm (Table 1), the length between approximately 20 and 160 mm (mean between 13.6 and ca. 37 mm) (Table 1). The ratio of the maximum to minimum diameter of the slices, F_{max} and F_{min}, respectively, varies from 1.6 to 3.3, with mean values between 2.08 and 2.84 (Table 1). In general the slices tend to decrease in length and thickness towards the fault core (particularly mean F_{max} decreases from approximately 37 to 18 mm) (Table 1). The F_{max}/F_{min} ratio, however, seems to attain constant values (within a 1σ standard
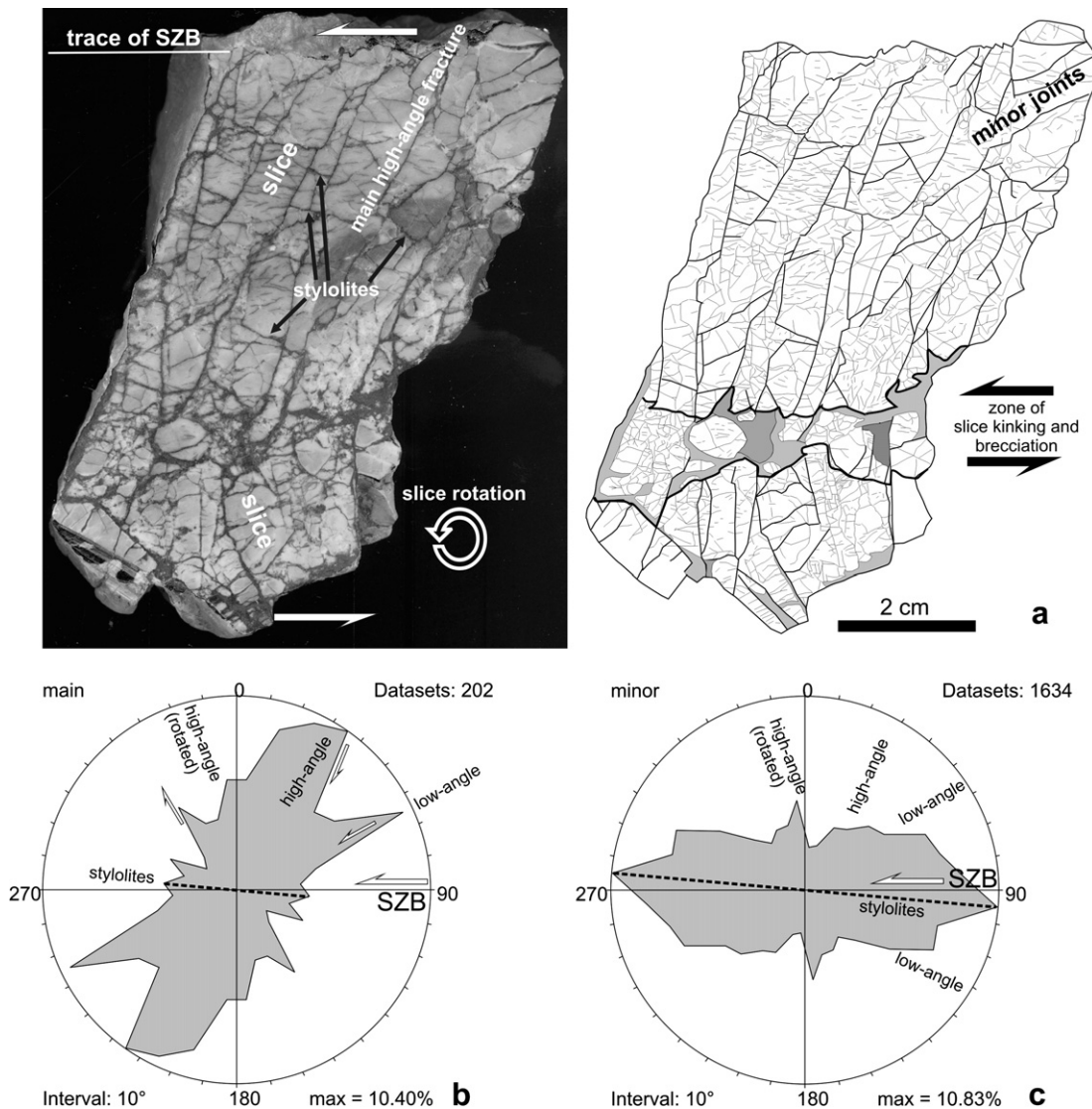

Fig. 6. (a) Polished and stained sample sections showing the fracture pattern of carbonate rocks along the Talhof fault damage zone–fault core transition. The distance to the damage zone–fault core boundary is approximately 30 cm. The shear zone boundary (SZB) runs parallel to the bedding/foliation. Thick lines: main fractures, thin lines: minor joints (modified after Brosch and Kurz, 2008). The Rose diagrams display the orientation of the distribution of slice-bounding (main) (b) and slice-internal (minor) (c) fractures relative to the SZB. Note the predominance of low angle and SZB-parallel minor shears. The slices are kinked and fractured related to a sinistral sense of shear along the SZB. The fracture zone is characterized by the formation of slice-derived fragments embedded within a finer-grained carbonate matrix. The shear sense within the fracture zone coincides with the general sense of shear along the SZB. Arrows indicate the displacement along reactivated structural elements. Sample from site "Stiegerinhütte" (see Appendix). See Fig. 3 for sampling site.
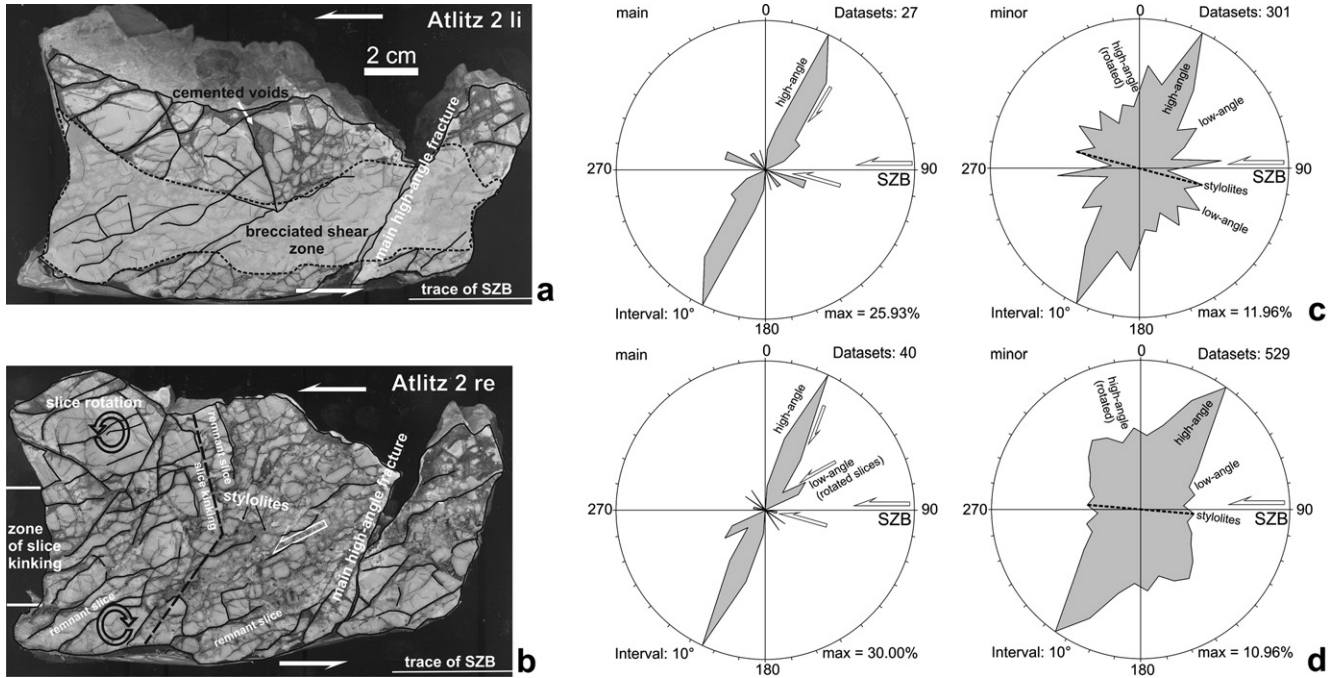
Fig. 7. (a), (b) Polished and stained sample sections showing the fracture pattern within carbonate rocks along the Talhof fault damage zone at a distance of approximately 25 cm (a) and 20 cm (b) to the damage zone–fault core contact, showing the increasing rotation of joint-bounded slices along a zone of slice kinking and fracturing towards the fault core. In the lower parts of the samples slices rotate into a low-angle orientation as well. Thick lines: slice-bounding (main) fractures, thin lines: slice-internal (minor) fractures. The shear zone boundary (SZB) runs parallel to the bedding/foliation. (c), (d) The Rose diagrams display the orientation of the distribution of main and minor fractures relative to the SZB. Arrows indicate the displacement along reactivated structural elements. Sample from site "Atlitz" (see Appendix).
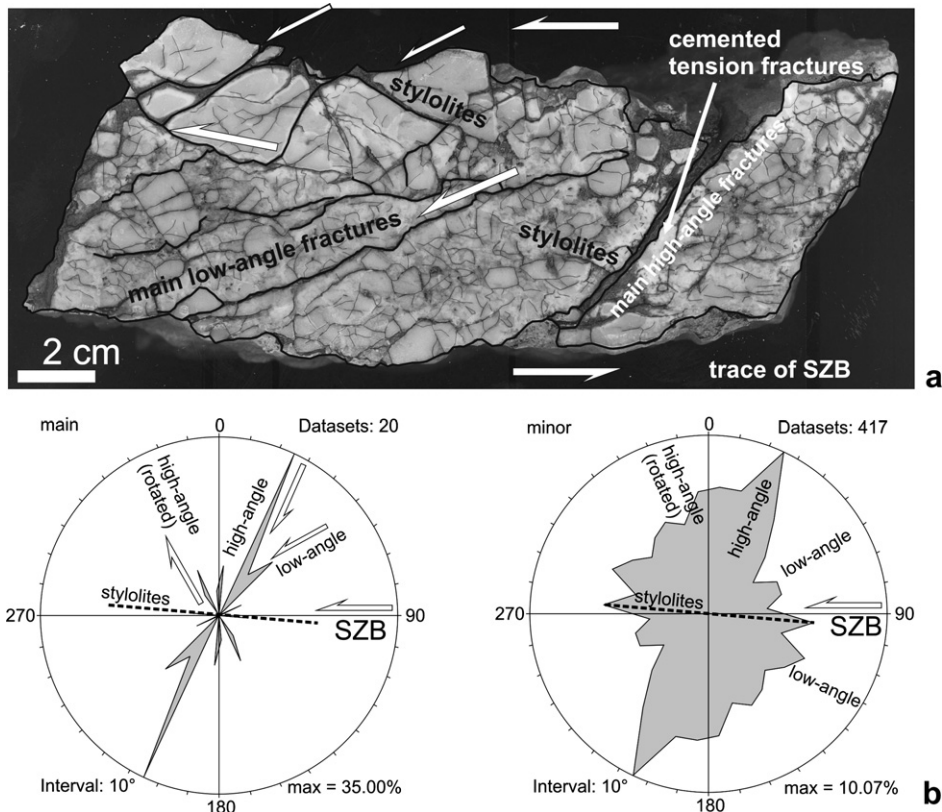

Fig. 8. Polished and stained sample sections showing the fracture pattern within carbonate rocks along the Talhof fault damage zone at a distance of approximately 15 cm (a) and 10 cm (b) to the damage zone–fault core contact, showing the increasing occurrence of main joint-bounded slices at a low-angle orientation to the SZB, and the subsequent development of slice-internal fractures, mainly at a high-angle orientation anticlockwise from the SZB. Stylolites predominantly form at low angles, 10–15° clockwise to the SZB. thick lines: slice-bounding (main) fractures, thin lines: slice-internal (minor) joints. Also note the increasing fragmentation of joint-bounded slices related to the formation of minor joints. The SZB runs parallel to the bedding/foliation. (c), (d) The Rose diagrams display the orientation of the distribution of main and minor fractures relative to the SZB. Arrows indicate the displacement along reactivated structural elements. Sample from site "Atlitz" (see Appendix).
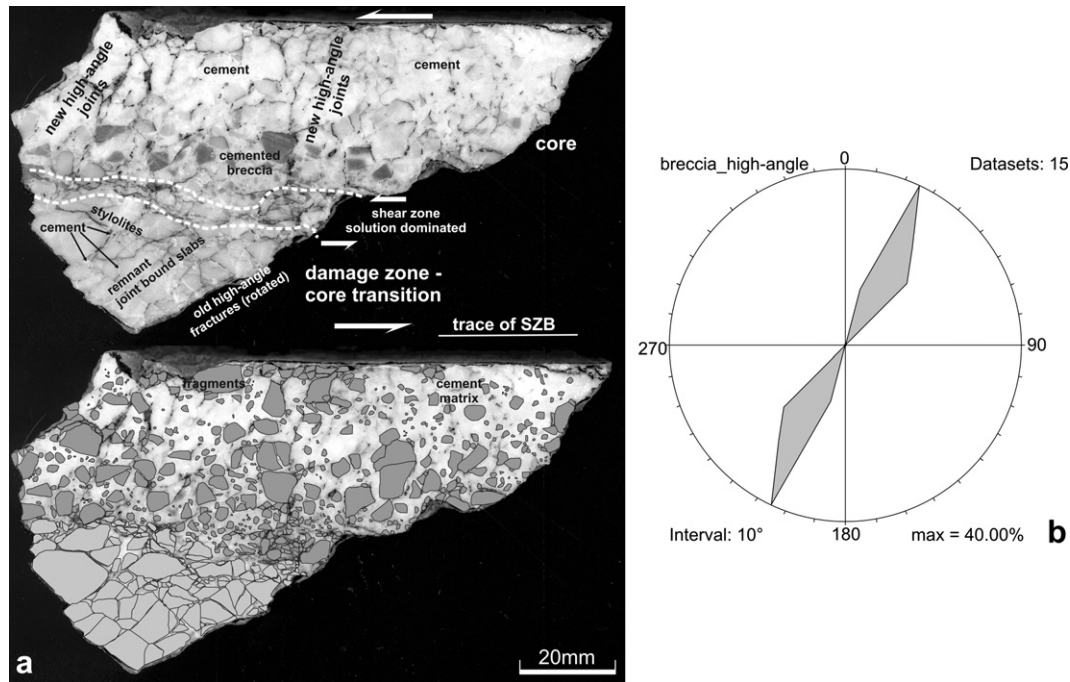
Fig. 9. (a) Polished and stained sample sections showing the cemented fault core breccia, with analysed cataclasite fragments (below) (sample Talhof 5, site "Stiegerinhütte"). The domain in the lower part of the sample mainly comprises fragmented joint-bounded slices, the domain in the upper part a mainly matrix-supported cataclasite. These domains are separated by a zone of closely spaced stylolites. The shear zone boundary (SZB) runs parallel to the bedding/foliation. Stylolites predominantly form at low angles, 10–15° clockwise to the SZB. Note that the cemented breccia is crosscut by high-angle joints at an orientation of 75° anti-clockwise from the SZB. (b) The Rose diagram displays the orientation of the distribution of high-angle joints crosscutting the cemented fault breccia. For sample site see Appendix and Fig. 3. Arrows indicate the displacement along reactivated structural elements.

deviation) between 2.8 and 2.3 (Table 1). Concerning the general shear direction along the SZB, most slices exhibit antithetic displacements along sheared joints and shear fractures. Voids and pull aparts along the sheared planes are partly healed with sparitic calcite cement (Fig. 4).

Most slices show an internal fabric formed by low- and high-angle joints (Figs. 4–7). Since these joints are only present within individual slices, they are considerably shorter (average length of 1–2 cm) than the slice-bounding sheared fractures. These internal fractures do not show any considerable displacement and usually terminate against slice-bounding fractures. In this study these fracture sets are described as minor joints. The maximum and minimum diameters (F_{max}, F_{min}) of fragments surrounded by these range from 2 to 10 and 1 to 6 mm, respectively, with a mean between 3.6 and 9.6 mm for the maximum (F_{max}) and 2 and 4.8 mm for the minimum diameter (F_{min}). The F_{max}/F_{min} ratios show mean values between 1.60 and 2.40, and a bulk mean value of 1.94 ± 0.69 (Table 1). With decreasing distances to the fault core, the slice-internal structure is dominated by low-angle joints, with a maximum frequency oriented at angles between 5 and 30° (Fig. 6b, c). Additional joint orientations turn up at 75°, 100°, and 120° anticlockwise to the SZB (see rose diagrams in Figs. 4–7).

Along distinct 0.5–2 cm thick zones oriented sub-parallel to the SZB, the slices are fractured perpendicular to their long axes, resulting in the formation of secondary slices and slice rotation (Figs. 4–7). Prior to the slice fracturing, the slices were rotated in an anti-clockwise sense (i.e. synthetically to the general shear direction). This resulted in the dragging of the slices along the SZB and anticlockwise shearing along the slice boundaries (Fig. 5a, b). Kinking of slices occurs along irregularly confined domains, oriented sub-parallel to the SZB. Within these domains, slices are irregularly fractured and broken up to fragments, which are embedded within a fine-grained matrix of crushed host rock

material or within sparitic carbonate cement (Figs. 4a, 6a). The fragments show an isometric shape with angular to sub-rounded boundaries. Fragment interfaces may show displacement at the scale of millimeters. Pressure solution seams (stylolites) are formed along fragment contacts aligned sub-parallel, or at low angles, to the planes of slice fragmentation or SZB (Figs. 4a, 6a). Locally, a completely developed matrix-supported fault breccia characterized by structural features indicating fragment wear, attrition, and fragment rotation developed within and between the slice domains. The matrix consists of fine-grained carbonate and residual clay minerals in the clay/silt grain size fractions.

At the damage zone–fault core transition, the slice-dominated fabrics described above are obliterated by increasing fragmentation due to development of fractures at low angles to the SZB (samples Atlitz2 and Atlitz1) (Figs. 7, 8). The partly dismembered survivor slices show an antithetic rotation of more than 30° from the initial slice orientation. Besides rotation, the slices were affected by fragmentation and fragment rotation, which resulted in the development of voids and veins (Figs. 7a, b, 8a) partly filled with sparitic cement, fine-grained carbonate, and pulverized carbonate in the clay/silt grain size fractions. Along the damage zone fault core boundary, as displayed by samples Atlitz1 and Atlitz2, F_{max} and F_{min} of joint-bounded slices are significantly smaller than in the samples described above. In particular F_{max} decreases due to fragmentation. In these domains, F_{max} reaches mean values between 13.6 and 17.7 mm (Table 1), so the F_{max}/F_{min} ratio is about 1.7 (Table 1).

7. Fault rocks along the damage zone–fault core boundary

The fault rocks (coarse-grained cataclasite, fault breccia) are characterized by an irregular grain size distribution (Figs. 9, 10). Sample SHWK2 is entirely made up of a medium-grained cemented cataclasite. Sample Talhof5 is characterized by two distinct

Table 1
Maximum (F_{max}) and minimum (F_{min}) diameters of fracture-bounded fragments from samples taken along the Talhof fault damage zone. The diameters were determined by measuring the distances between two parallel tangents to the fragment margins at opposite points. Exemplified for sample Talhof3 the dimensions of fragments bounded by minor joints are displayed as well (data from the other samples are not displayed here mainly for space reasons, but are available from the corresponding author). For the bulk samples the F_{max}/F_{min} ratios obtain a constant value around 2 within the 1σ standard deviation. DZ: damage zone.

	Structural position	Mean F_{max} (mm)	std. dev. (1σ)	F_{min} (mm)	std. dev. (1σ)	Mean F_{max}/F_{min}	std. dev. (1σ)	Fragment quantity
Main fractures								
Sample								
Talhof3	DZ–core transition	17.47	9.08	7.47	2.87	2.27	0.70	13
Atlitz_re1	DZ–core transition	17.73	9.35	9.52	6.50	2.24	0.78	9
Atlitz2_li	DZ–core transition	13.63	7.66	8.29	4.95	1.71	0.38	12
Atlitz2_re	DZ–core transition	16.92	8.17	9.85	5.74	1.80	0.43	14
Atlitz3_li	DZ	19.35	11.23	7.97	3.77	2.42	0.80	20
Atlitz3_re	DZ	33.85	33.56	14.86	9.37	2.08	0.66	8
Atlitz4_li	DZ	36.88	13.62	15.03	7.03	2.58	0.59	9
Atlitz4_re	DZ	27.70	18.34	9.60	4.54	2.84	0.95	11
Atlitz5_li	DZ	26.10	8.80	11.82	5.88	2.46	0.88	10
Atlitz5_re	DZ	26.07	9.03	10.90	3.89	2.41	0.25	6
Minor fractures								
Talhof3	Damage zone–core transition							
Internal		5.14	1.91	2.63	1.09	2.02	0.53	18
Internal		3.87	2.08	1.98	1.23	2.15	0.87	24
Internal		4.95	2.52	2.99	1.81	1.88	0.67	8
Internal		4.07	0.73	2.16	0.56	1.97	0.49	9
Internal		6.65	3.86	2.88	1.82	2.40	0.62	11
Internal		3.86	1.21	2.28	0.46	1.68	0.32	8
Internal		4.35	1.59	2.05	0.63	2.16	0.54	16
Internal		4.81	2.20	2.55	1.30	2.03	0.71	42
Internal		4.46	3.11	3.61	1.83	1.87	0.46	6
Internal		3.58	0.60	2.33	0.76	1.60	0.33	7
Internal		5.04	1.8	2.66	1.11	2.07	0.85	23
Internal		6.14	1.72	2.89	1.16	2.20	0.28	3
Internal		4.67	2.02	2.46	0.61	1.89	0.57	19
Bulk		4.61	2.20	2.41	1.17	1.94	0.69	194
Atlitz_re1	DZ–core transition	7.34	5.25	4.3	3.06	1.76	0.50	113
Atlitz2_li	DZ–core transition	8.73	4.79	4.74	2.64	1.90	0.53	103
Atlitz2_re	DZ–core transition	7.66	4.44	4.01	1.94	1.95	0.63	166
Atlitz3_li	DZ	8.10	4.46	4.35	2.16	1.96	0.70	211
Atlitz3_re	DZ	8.21	3.51	4.27	2.06	2.05	0.63	150
Atlitz4_li	DZ	9.63	4.94	4.71	2.36	2.14	0.72	145
Atlitz4_re	DZ	8.17	3.79	4.42	2.27	1.96	0.55	171
Atlitz5_li	DZ	8.64	4.45	4.53	2.27	2.01	0.64	135
Atlitz5_re	DZ	8.45	3.86	4.77	2.41	1.86	0.55	177

domains (Fig. 9). The portions immediately adjacent to the fault plane consist of medium-grained carbonate cataclasites, while those near the damage zone grade into a grain-supported fault breccia. Remnants of former joint-bounded slices are still observable (Fig. 9a). The fragments are characterized by polygonal shapes and show irregular, angular to slightly rounded, boundaries.

The fault rocks show an exponential fragment size distribution (Fig. 10). Within the cemented cataclasite, the size of the fragments varies between 0.1 and 11 mm (F_{max}), with a mean of 1.74 mm, and between 0.05 mm and 6.5 mm (F_{min}), with a mean of 1.03. Fragment to fragment contacts are observed only close to the damage zone and are rare towards the fault core. The section area covered by fragments within the cemented cataclasites averages approximately 33.5–38%. This fault rock is crosscut by joints at 70–80°

anticlockwise from the SZB (Fig. 9). These joints are spaced at approximately 1 cm, resulting in the development of new joint-bounded slices within the cataclasites (Fig. 9a).

The transition from the cataclasite to the damage zone is marked by pressure solution seams. These stylolitic fabrics are oriented at low angles to the SZB (Fig. 9a). In this domain (below the shear zone indicated in Fig. 9a) relics of slices can be observed, rotated by 30–50° in a clockwise sense with regard to their original orientation. The size of the fragments formed by these structures varies between 0.1 mm and 16 mm (F_{max}), with a mean of 3.18 mm, and between 0.05 mm and 10.8 mm (F_{min}), with a mean of 1.69. The aspect ratio of the fragments (F_{max}/F_{min}) varies between 1.1 and 5.2, with a mean of 1.99. The section area covered by fragments averages approximately 60–78%. These domains are also characterized by an exponential fragment size distribution. The distribution, however, is more homogenous (Fig. 10).

8. Oxygen and carbon stable isotope compositions

Powder samples were obtained by microdrilling of the rock specimens described above. These samples were analysed using stable isotope geochemistry in order to determine the isotopic composition of (1) host rock-derived slices within the damage zone (Figs. 4–9), of (2) cataclasite fragments and of (3) fault rock cements (Fig. 9). The analytical techniques are described in the Appendix. Carbon and oxygen isotopic ratios are plotted in Fig. 11 and listed in Table 2. $\delta^{13}C$ and $\delta^{18}O$ isotope analysis provides the characterization of the isotopic signature of fault-related calcites, and the origin of the fluids from which these calcite phases were precipitated (e.g., Kerrich, 1986; Pili et al., 2002).

The slice-dominated samples show two different types of sparitic cement located in voids and pull aparts between the fracture-bounded slices. The slice fragments have carbon ($\delta^{13}C$) and oxygen ($\delta^{18}O$) isotope values ranging from +3.18‰ to 3.46‰ and −6.52‰ to −6.71‰, respectively. The cement isotopic data define a trend in the $\delta^{13}C$–$\delta^{18}O$ diagram with increasing $\delta^{13}C$ values and decreasing $\delta^{18}O$ values towards the fault core (Fig. 11). The cement composition varies between −2.46‰ and −2.98‰ ($\delta^{13}C$) and −5.19‰ to −6.35‰ ($\delta^{18}O$) (white sparitic cement), and −0.71‰ to −0.81‰ and −5.47‰ to −5.90‰ (red cement), respectively. Within the fault rocks the isotope composition of the fragments ranges from approximately 0.5‰ to 2.9‰ ($\delta^{13}C$) and −5.7‰ to −7.8‰ ($\delta^{18}O$). The cement isotope compositions show $\delta^{13}C$ values of −0.26‰ to 1.08‰ and $\delta^{18}O$ values of −6.4‰ to −9.4‰. The relatively low $\delta^{13}C$ and $\delta^{18}O$ values are typical for carbonate rocks that have precipitated from, or exchanged with, meteoric water at low temperatures (e.g., Kerrich, 1986; Ghisetti et al., 2001). The rather tight range of $\delta^{13}C$ values in cements rules out the incorporation of carbon from low $\delta^{13}C$ organic sources (e.g., Kerrich, 1986).

In general, the cements between slice fragments show significantly lower $\delta^{13}C$ values compared to the $\delta^{13}C$ isotopic composition of the protolith slices. Cements from the cataclasites, however, show a $\delta^{13}C$ isotopic composition more similar to the protolith slices, suggesting that the carbon was derived from the latter.

Cements between host rock-derived slices are depleted in $\delta^{18}O$ with respect to the slices, whereas calcite veins crosscutting cemented cataclasites are partly enriched in $\delta^{18}O$. Matrix cement from the cataclasites show a similar $\delta^{18}O$ composition with respect to the host rock-derived fragments, being consistent with local isotopic equilibrium between the cement-forming fluid and these fragments. This process was probably facilitated by the surface-controlled exchange between fluids and fine-grained fragments. The low $\delta^{18}O$ values of calcite veins with respect to the host rock-derived fragments indicate that calcite precipitated from fluids with either lower $\delta^{18}O$ composition or higher temperatures
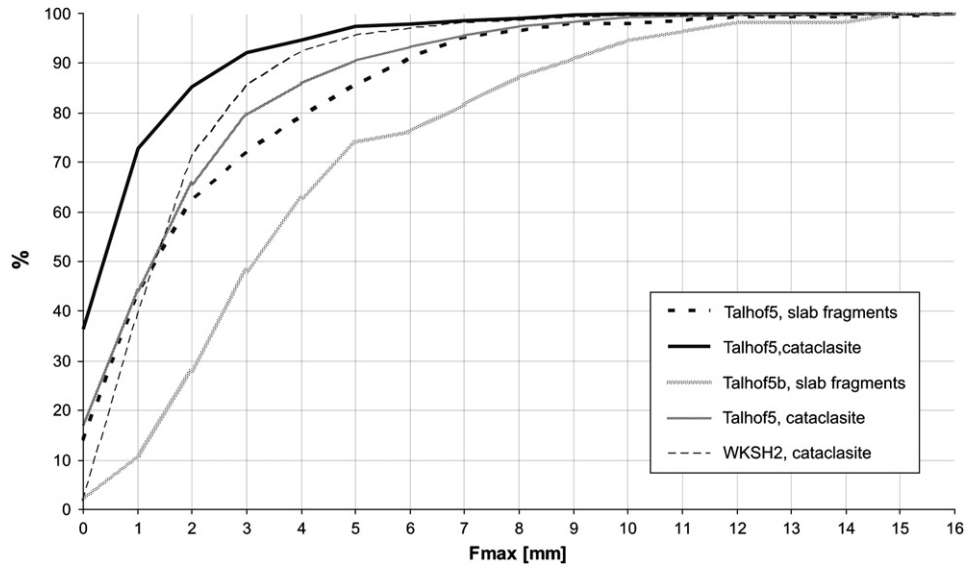
Fig. 10. Fragment size (maximum diameter F_{max}) distribution diagram (fragment size vs. bulk percentage of grains smaller than a given size) of fault core rocks. The sampling sites are displayed in Fig. 3. The distributions for samples Talhof5 and Talhof5b are given for separate domains, characterized by fragmented fracture-bounded slices and matrix-supported cemented cataclasite, respectively (see Fig. 9).

(e.g., Kerrich, 1986; Marquer and Burkhard, 1992). The similar carbon isotopic compositions of cataclasite fragments and surrounding cements could be due to a mineralizing fluid buffered with the adjacent surrounding cataclastic material (Marquer and Burkhard, 1992; Micarelli et al., 2005). The slight difference in $\delta^{13}C$ compositions may reflect the presence of a relatively open system.

9. Discussion of structural data

9.1. Implications for the formation of carbonate fault rocks

The structural evolution presented in this study (Fig. 12) is that fault zone development within layered carbonates starts with shearing of the primary composite foliation. This includes cross jointing between layer-parallel shears (Fig. 12a, b). These joints form a penetrative fabric in terms of a fracture cleavage, which is in contrast to some previous examples (e.g., Wilcox et al., 1973; Paterson, 1978; Olson and Pollard, 1991; Davis et al., 1999; Mandl, 2005). Example: (1) high-angle fractures of R′-orientation either form in domains of only partly overlapping fault segments (e.g., Naylor et al., 1986), or as (2) bridge structures (Gamond, 1983, 1987; Katz et al., 2004; Kim et al., 2004), or as (3) cross-joints between

en-echelon fractures in R-orientation (Mollema and Antonellini, 1999).

Strain accommodation was achieved by sliding along the SZB (foliation planes) (Fig. 12a), cross jointing and bookshelf rotation of joint-bounded slabs with antithetic shearing of high-angle joints (Fig. 12b). The subsequent fracturing and kinking of slices (Fig. 12c) suggests that the widening of the shear zone was inhibited (e.g., Means, 1995) due to the high ratio between the effective normal stress acting perpendicular to the externally imposed general shear direction ($\sigma_\perp$) and the normal stress acting parallel to that direction (σ_{II}) (e.g., Mandl, 1988, 2000; Wibberley et al., 2000; Brosch and Kurz, 2008) (Fig. 12b, c). Accordingly, the maximum principal stress is assumed to be oriented at very high angles to the SZB. This is supported by the original high-angle orientation of joints, and by the orientation of stylolites at low angles to the SZB.

The formation of high-angle fractures is interpreted to represent the initial states in shear zone development and results in the linkage of the pre-existing layer-parallel discontinuities (Crider and Peacock, 2004). The slices originally bounded by joints approach a constant shape and geometry, defined by the F_{max}/F_{min} ratio (Table 1). In general, this ratio lies between 2.8 and 2.1, with a mean value of approximately 2.3. This ratio decreases towards the fault
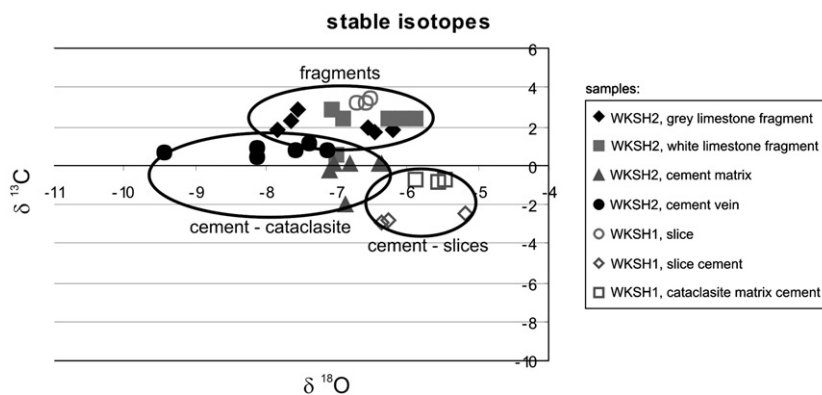

Fig. 11. Stable isotope compositions ($\delta^{13}C$ and $\delta^{18}O$ in ‰) of host rock slices from the fault damage zone, fault rock fragments and fault rock cements from the fault core, showing the concordance of cement isotope signatures with increasing fragmentation, i.e. from slice to cataclasite formation. Sample WKSH2 is a matrix-supported cataclasite, WKSH1 consists of cemented fractured slices, both according to the domain description in Fig. 9. The sampling sites are displayed in Fig. 3.
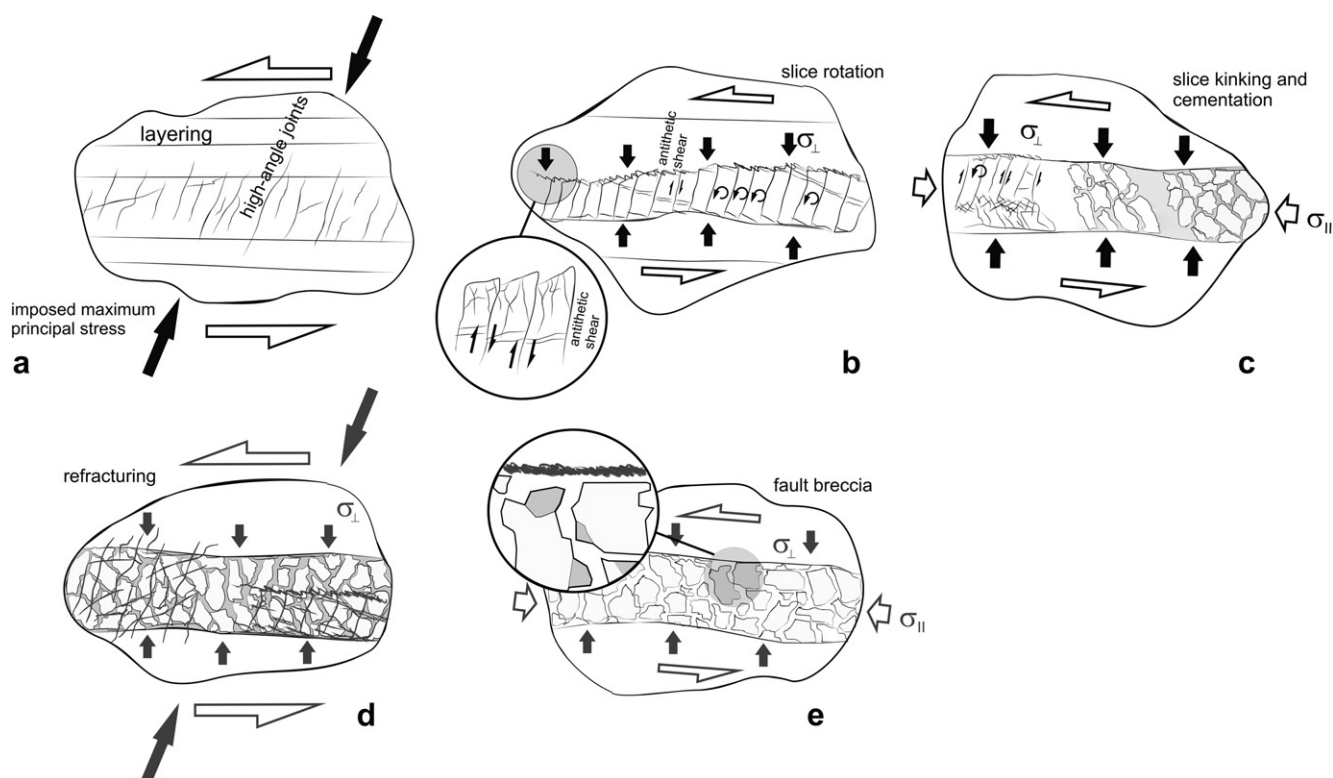
Fig. 12. Schematic model of shear zone evolution during layer-parallel shear along the Talhof fault deduced from field and sample observations (modified after Brosch and Kurz, 2008). (a) Formation of distinct cross-joints at high angles to the pre-existing bedding/foliation planes. (b) Formation of joint-bounded slices, rotation of slices, reactivation of joints as shears with antithetic displacement, and formation of secondary joints at the tips and internal parts of slices. Widening of the fault zone is inhibited by external compressive stresses at high angles to the SZB, stylolites are formed at low angles to the SZB, perpendicular to maximum principal stress orientation. (c) Kinking, fracturing and disintegration of slices by bookshelf rotation, developing into a cataclastic shear zone at advanced stages of displacement. (d) Cementation of disintegrated slices and subsequent formation of new high-angle joints. (e) Second cycle of brecciation. The newly formed fragments consist of both slice fragments and fragments of sparitic cement. $\sigma_\perp$: effective normal stress acting perpendicular to the externally imposed general shear direction. σ_{II}: effective normal stress acting parallel to the externally imposed general shear direction.

core. In particular, F_{max} shows a strong decrease due to fragmentation and the F_{max}/F_{min} ratio lowers to values of 1.7 (Table 1). The detection of isolated slice fragments within the fault breccia indicates that these were progressively incorporated into the fault core. Within the fault core cataclasites, however, the mean fragment size decreases continuously (Fig. 10). Following Billi et al. (2003a), rocks in damage zones adjacent to fault cores show very similar structural fabrics and consist of nearly isometric lithons with a cross-sectional aspect ratio of about 1.4 (despite different sizes, kinematics, and inherited structural fabrics of the protolith), being the upper limit for the initiation of particle rotation and grinding within cataclasites.

9.2. Mechanisms of deformation and grain size reduction

Calcite mainly deforms by fracturing, jointing, grain size-sensitive processes such as solution transfer and grain-boundary sliding (Kennedy and Logan, 1998; Kennedy and White, 2001; Mazzoli et al., 2001), and twinning (e.g., Burkhard, 1993) at temperatures below 250 °C. The formation of joints, as well as kinking and cracking of joint-bounded slices, enabled the inflow of fluids into the fault zone. Vice versa, the presence of fluid phases and related fluid pressures generally decreases the effective normal stresses and therefore facilitates fracturing of rocks (e.g., Sibson et al., 1975; Sibson, 1981, 1990, 1992, 1996; Ramsay, 1980; Byerlee, 1993; Janssen et al., 1998; Petit et al., 1999; Tenthorey et al., 2003; Agosta and Aydin, 2006; Smith et al., 2008). Fracturing generally results in a reduction of internal stresses within the rock mass, and a reduction of pore fluid pressure (e.g., Sibson et al., 1975; Ramsay, 1980). The presence of fluids within the fault zone results in a decrease of

shear stresses until the precipitation of solid phases, such as sparitic cement, is initiated. Healing and cementation of the fault zone increase the cohesive strength in terms of hardening and shift the failure envelope to higher values with time. Precipitation of sparitic cements can therefore change the strength and behaviour of fault zones via crack healing and sealing (Sibson et al., 1975; Ramsay, 1980; Sibson, 1996; Tenthorey et al., 2003; Tarasewicz et al., 2005; Yasahuara et al., 2005; Collettini et al., 2006; Woodcock et al., 2007).

The formation of matrix-supported cataclasites suggests that the highly fractured material along the damage zone–fault core boundary behaved similar to loose, granular material deformed by cataclastic flow (e.g., Smith et al., 2008). Subsequent cementation of cataclasites, however, resulted in strain hardening with the subsequent formation of new joints at high angle anticlockwise from the SZB (Figs. 9, 12d, e). Joint formation may therefore be described as a cyclic process of cementation, healing, and re-fracturing (Woodcock et al., 2007). Multiple cyclic fracturing is therefore an important mechanism for the development of isometric grain shapes, and for grain size reduction of host rock-derived fragments within carbonate fault rocks (Figs. 9, 10). Hardening of the carbonates, however, resulted in the shifting of shear localization towards the un-cemented quartzitic domains, now forming the main fault core. Consequent shear localization in these domains resulted in the development of quartz gouges in fault core domains 2–4 (Fig. 3).

9.3. Implications for fluid–rock interaction and fluid flow

Stable isotope geochemistry provides hints on the origin of the fluids, the fluid–rock ratio, and fluid–rock interaction within and

Table 2
Stable isotope composition of host rock lamellae within the Talhof fault damage zone, fault rock fragments and fault rock cements.

Sample		$\delta^{18}O$ (‰)	$\delta^{13}C$ (‰)
WKSH2K11	Grey limestone fragment	−7.82	1.88
WKSH2K12	Grey limestone fragment	−7.55	2.91
WKSH2K13	Grey limestone fragment	−7.64	2.28
WKSH2K11-1	Grey limestone fragment	−6.21	1.85
WKSH2K11-2	White limestone fragment	−6.56	1.97
WKSH2K11-3	White limestone fragment	−6.45	1.72
WKSH2K14	White limestone fragment	−7.07	2.83
WKSH2K15	White limestone fragment	−6.92	2.44
WKSH2K16	White limestone fragment	−7.01	0.53
WKSH2K15-1	White limestone fragment	−6.26	2.36
WKSH2K15-2	White limestone fragment	−6.07	2.40
WKSH2K15-3	White limestone fragment	−5.87	2.36
WKSH2Z9	Sparitic cement	−6.88	−2
WKSH2Z10	Sparitic cement	−7.05	0.05
WKSH2Z11	Sparitic cement	−7.1	−0.26
WKSH2Z10-1	Sparitic cement	−6.36	0.08
WKSH2Z10-2	Sparitic cement	−6.40	0.04
WKSH2Z10-3	Sparitic cement	−6.80	0.03
WKSH2Z12	Sparitic cement	−8.12	0.85
WKSH2Z13	Sparitic cement	−9.42	0.65
WKSH2Z14	Sparitic cement	−8.12	0.38
WKSH2Z12-1	Sparitic cement	−7.12	0.82
WKSH2Z12-2	Sparitic cement	−7.58	0.79
WKSH2Z12-3	Sparitic cement	−7.38	1.08
WKSH1-K-1	Slab	−6.60	3.19
WKSH1-K-2	Slab	−6.71	3.18
WKSH1-K-3	Slab	−6.52	3.46
WKSH1Z-1	White cement between slice	−6.26	−2.86
WKSH1Z-2	White cement between slice	−6.35	−2.98
WKSH1Z-3	White cement between slice	−5.19	−2.46
WKSH1RZ-1	Red cement between fragments	−5.47	−0.75
WKSH1RZ-2	Red cement between fragments	−5.57	−0.81
WKSH1RZ-3	Red cement between fragments	−5.90	−0.71

along the fault zone. The carbon ($\delta^{13}C$) and oxygen ($\delta^{18}O$) isotope values of un-altered damage zone slices reflect the original host rock signature. The cataclasite fragments within the fault core show a similar isotope composition for $\delta^{18}O$. In contrast, several cements between joint-bounded slices deviate significantly from this isotope signature (Fig. 11; Table 2).

Within the cataclasites, the cement isotope compositions are closer to the signature of the host rock fragments (Fig. 11; Table 2). The rather large range of the $\delta^{18}O$ isotopic composition of cements may also indicate a repeated infiltration of different fluids (Janssen et al., 1998). The light $\delta^{18}O$ values for calcite veins (Fig. 11) are typical of a meteoric-derived fluid from a near-surface source (e.g., Kerrich, 1986). As the fluid that entered the fault zone usually shows a constant isotope composition, the relative position of the individual datum in the $\delta^{13}C$ and $\delta^{18}O$ trend is more related to variations in the amount of fluids (Kirschner and Kennedy, 2001; Pili et al., 2002; Agosta and Kirschner, 2003). Samples with isotopic values similar to the carbonate host rocks either interacted with small quantities of fluid, or precipitated from a fluid that had previously equilibrated with the host rock. Conversely, samples with lower isotopic values either interacted with larger quantities of fluid, or precipitated from a fluid that had partly retained its original isotopic values (Agosta and Kirschner, 2003).

The isotopic signatures indicate four main points:

(1) Within the damage zone, a high fluid–rock ratio prohibited the complete isotopic homogenization between host rock-derived slices and fluids. This might alternatively also be interpreted in terms of enhanced fluid flow along, or across, the damage zone rather than in terms of a stagnating fluid.
(2) Within the cataclasites, the fluid–rock ratio was low, resulting in a buffered isotopic signature composition. Alternatively, the

reduced fragment size, and increased surface area within the cataclasites caused this isotope homogenization.
(3) The fact that only a few joints are healed while all cataclasites are cemented suggests either a rapid opening of joints (hydraulic fracturing) (Beach, 1980; Ramsay, 1980; Sibson, 1981), or preferential fluid flow within the fault core (Busso-lotto et al., 2007), or that these partly healed joints are later structures.
(4) Meteoric water is one of the more common fluids in the earth's crust with sufficiently low $\delta^{13}C$ and $\delta^{18}O$ values to account for the low isotopic values of calcite precipitated at low temperatures (Kerrich, 1986; Marquer and Burkhard, 1992; Janssen et al., 1998; Agosta and Kirschner, 2003). Although not definitive, the incursion of deeply sourced CO_2-bearing fluids (e.g., from mantle, or metamorphic decarbonation of limestones) into the studied fault zone is neither supported by the observed structures, nor from the isotopic data

Within the fault zone carbonates, the large range in $\delta^{18}O$ values indicates considerable fluid–rock interaction. Cementation and sealing may also have resulted in diminishing the replenishment of fluids into the carbonates, but increased infiltration of the adjacent quartzite domains. The negligible contents of carbonate cements in domains 2–4 (Fig. 3) (Kiechl, 2007) also indicate that these domains were not infiltrated by carbonate-bearing fluids from the adjacent domain 1, and that quartz gouges in domains 2–4 probably acted as a barrier to fluid flow. These fluids were therefore entrapped in the carbonate domains along the damage zone–fault core boundary. Both cementation of fault core cataclasites and the adjacent barrier therefore favour an increase of fluid pressures in the carbonate damage zone domains, convenient for subsequent frictional failure along the fault core–damage zone boundary, and the development of a temporally open system being accessible for fluid infiltration.

10. Conclusions

(1) In layered rocks, formation of cataclastic shear zones may start with layer parallel shear and the development of cross-joints at high angles to the shear zone boundary (SZB). This results in the formation of joint-bounded, closely spaced slices, forming a penetrative fabric (fracture cleavage) at the scale of the shear zone.
(2) The formation of slices bounded by en-echelon joints at high angle to the SZB was probably related to the high ratio of effective normal stresses acting orthogonal to the normal stresses acting parallel to the SZB. Therefore, widening of the shear zone was inhibited.
(3) Subsequent slice rotation resulted in antithetic shearing along the slice-bounding joints. As shear zone widening was prohibited, strain was accommodated by the fracturing of slices along distinct zones parallel to the SZB.
(4) The transition to cataclastic flow is marked by rupturing along these fracture zones and breaking-up to smaller fragments with rotational and translational displacements. Subsequent shear is localized along these zones, ending up with the evolution of a fault core.
(5) Stable isotope compositions ($\delta^{13}C$ and $\delta^{18}O$) indicate that fault cements most probably precipitated from meteoric-derived fluids infiltrating the fault zone. The continuous homogenization of the isotope signatures from the damage zone towards the fault core indicates that the fluid–rock ratio in the fault core was lower than within the damage zone.
(6) Cementation and sealing resulted in reduction of porosity and permeability, reduction of fluid flow through the carbonates,

and in the development of a temporally closed system. This process led to shear localization in adjacent gouge domains.

(7) The formation of high-angle joints together with layer-parallel shear is interpreted to represent the initial states in the development of a brittle shear zone in anisotropic rocks.

(8) Formation of joint-bounded slices may proceed repeatedly in the case that breccias get cemented and undergo continuous brittle deformation in terms of cyclic healing and fracturing. This enforces the development of isometric shapes of host rock-derived fragments, and is a main mechanism of fragment size reduction.

(9) The cyclic change between fluid infiltration induced by brittle failure, and cementation implies a cyclic change between an open and a closed system.

(10) Fault sealing by cementation in carbonates is a main agent for strain hardening. Shear localization is therefore forced to shift to adjacent domains characterized by material properties which favour strain weakening.

Acknowledgements

Appendix

Analytical techniques

Oxygen and carbon isotope ratios were measured in the isotope lab of the Institute of Earth Sciences (University of Graz) with a "Delta-Plus" mass spectrometer equipped with a dual inlet system, and at the Joanneum Research Forschungsgesellschaft mbH (Graz, Austria). These systems provide a continuous-flow isotope ratio mass spectrometric analysis. Isotope extraction from calcite was performed using the commercial "Kiel II" system. The analyses were calibrated against NBS28 (quartz), and NBS18 (calcite) standards (IAEA). Oxygen data are displayed as $\delta^{18}O$ with respect to Standard Mean Ocean Water (SMOW).

Phosphoric acid is added dropwise into individual sample vials by a fully automated acid dosing system. The evolved CO_2 is slowly passed through a sampling loop in a trickling stream of helium. Repetitive loop injections onto an isothermal GC column create a series of pulses of pure CO_2 in He, which enter the IRMS via an open split. An overall precision of 0.08‰ for $\delta^{18}O$ and of 0.06‰ for $\delta^{13}C$ has been achieved.

Experimental conditions

Borosilicate sample bottles are washed in diluted acid, then twice in de-ionized water and overnight dried at 70 °C. After adding the samples to the vials in air, they are sealed using unused septa. Residual air is removed from the sample vials by automated autosampler-assisted flushing with He, using a flow of 100 ml/min of He for 5 min. The phosphoric acid, which is maintained at the reaction temperature, is added dropwise under computer control to each individual reaction vessel. In these experiments, 3 drops of acid were added to each sample prior to measurement. A reaction time of 60 min was used. Both the amount of the acid and the reaction time are controlled by the software.

Corrections applied for different sample sizes

Data were extracted to an EXCEL file by using the ISODAT NT EXCEL export utility and further calculation steps were carried out using a predefined EXCEL Worksheet. The small linear dependence of $\delta^{18}O$ on increasing peak intensities (within the linearity specifications of the DELTAplus) was corrected using a linearity factor (the slope of a line in m/z 44 intensity vs. $\delta^{18}O$). The slope determined is small for $\delta^{18}O$ (0.015‰/nA). For $\delta^{13}C$, no slope correction was applied.

Coordinates of sites and sampling locations:

Stiegerinhütte": Topographic map of Austria, 1:50,000, sheet no. 104 (Mürzzuschlag); 15° 44′ 29″ E; 47° 39′ 17″ N.

Atlitz": Topographic map of Austria, 1:50,000, sheet no. 104 (Mürzzuschlag); 15° 47′ 23″ E; 47° 39′ 28″ N.

References

Agosta, F., Aydin, A., 2006. Architecture and deformation mechanism of a basin-bounding normal fault in Mesozoic platform carbonates, central Italy. Journal of Structural Geology 28, 1445–1467.

Agosta, F., Kirschner, D.L., 2003. Fluid conduits in carbonate-hosted seismogenic normal faults of central Italy. Journal of Geophysical Research 108 2002JB002013.

Anderson, E.M., 1951. The Dynamics of Faulting. Oliver & Boyd, Edinburgh, 206 pp.

Beach, A., 1980. Numerical models of hydraulic fracturing and the interpretation of syntectonic veins. Journal of Structural Geology 2, 425–438.

Billi, A., 2005. Grain size distribution and thickness of breccia and gouge zones from thin (<1 m) strike-slip fault cores in limestone. Journal of Structural Geology 27, 1823–1837.

Billi, A., 2007. On the extent of size range and power law scaling for particles of natural carbonate fault cores. Journal of Structural Geology 29, 1512–1521.

Billi, A., Salvini, F., Storti, F., 2003a. The damage zone–fault core transition in carbonate rocks: implications for fault growth, structure and permeability. Journal of Structural Geology 25, 1779–1794.

Billi, A., Storti, F., Salvini, F., 2003b. Particle size distributions of fault rocks and fault transgression: are they related? Terra Nova 15, 61–66.

Billi, A., Storti, F., 2004. Fractal distribution of particle size in carbonate cataclastic rocks from the core of a regional strike-slip fault zone. Tectonophysics 384, 115–128.

Brodie, K., Fettes, D., Harte, B., Schmid, R., 2002. Structural Terms Including Fault Rock Terms. IUGS Subcommission on the Systematics of Metamorphic Rocks, 8 pp.

Brosch, F.J., Kurz, W., 2008. Fault damage zones dominated by high-angle fractures within layer-parallel brittle shear zones: examples from the Eastern Alps. In: Geological Society of London Special Publication, vol. 299 75–95.

Burkhard, M., 1993. Calcite twins, their geometry, appearance and significance as stress–strain markers and indicators of tectonic regime: a review. Journal of Structural Geology 15, 355–368.

Bussolotto, M., Benedicto, A., Invernizzi, C., Micarelli, L, Plagnes, V., Deiana, G., 2007. Deformation features within an active normal fault zone in carbonate rocks: the Gubbio fault (Central Apennines, Italy). Journal of Structural Geology 29, 2017–2037.

Byerlee, J., 1993. Model for episodic flow of high-pressure water in fault zones before earthquakes. Geology 21, 303–306.

Caine, J.S., Evans, J.P., Forster, C.B., 1996. Fault zone architecture and permeability structure. Geology 24, 1025–1028.

Caine, J.S., Foster, C.B., 1999. Fault zone architecture and fluid flow: insights from field data and numerical modelling. In: Haneberg, W.C., Mozley, P.S., Moore, J.C., Goodwin, L.B. (Eds.), Faults and Subsurface Fluid Flow in the Shallow Crust. Geophysical Monograph, vol. 113. American Geophysical Union, pp. 101–127.

Chester, F.M., Evans, J.P., Biegel, R.L., 1993. Internal structure and weakening mechanisms of the San Andreas. Journal of Geophysical Research 98, 771–786.

Chester, F.M., Logan, J.M., 1986. Implications for mechanical properties of brittle faults from observations of the Punchbowl Fault, California. Pure and Applied Geophysics 124, 79–106.

Chester, F.M., Logan, J.M., 1987. Composite planar fabric of gouge from the Punch-bowl Fault, California. Journal of Structural Geology 9, 621–634.

Chester, F.M., Logan, J.M., 1990. Frictional faulting in polycrystalline halite: correlation of microstructure, mechanism of slip and constitutive behavior. American Geophysical Monographs 56, 49–56.

Collettini, C., De Paola, N., Holdsworth, R.E., Barchi, M.R., 2006. The development and behaviour of low-angle normal faults during Cenozoic asymmetric extension in the Northern Apennines, Italy. Journal of Structural Geology 28, 333–352.

Crider, J.G., Peacock, D.C.P., 2004. Initiation of brittle faults in the upper crust: a review of field observations. Journal of Structural Geology 26, 691–707.

Davis, G.A., Bump, A.P., Garcia, P.E., Ahlgren, S.G., 1999. Conjugate Riedel deformation band shear zones. Journal of Structural Geology 22, 169–190.

Decker, K., Meschede, M., Ring, U., 1993. Fault slip analysis along the northern margin of the Eastern Alps (Molasse, Helvetic nappes, North and South Penninic flysch, and Northern Calcareous Alps). Tectonophysics 223, 291–312.

Decker, K., Peresson, H., 1996. Tertiary kinematics in the Alpine–Carpathian–Pannonian system: links between thrusting, transform faulting and crustal extension. In: Wessely, G., Liebl, W. (Eds.), Oil and Gas in Alpidic Thrustbelts and Basins of Central and Eastern Europe. EAGE Special Publication, pp. 69–77.

Faulkner, D.R., Lewis, A.C., Rutter, E.H., 2003. On the internal structure and mechanics of large strike-slip fault zones: field observations of the Carboneras fault in southeastern Spain. Tectonophysics 367, 235–251.

Frisch, W., Dunkl, I., Kuhlemann, J., 2000. Post-collisional orogen-parallel large-scale extension in the Eastern Alps. Tectonophysics 327, 239–265.

Gamond, J.F., 1983. Displacement features associated with fault zones: a comparison between observed examples and experimental models. Journal of Structural Geology 5, 33–45.

Gamond, J.F., 1987. Bridge structures as sense of displacement in brittle fault zones. Journal of Structural Geology 9, 609–620.

Ghisetti, F., Kirschner, D.L., Vezzani, L., Agosta, F., 2001. Stable isotope evidence for contrasting paleofluid circulation in thrust faults and normal faults of the central Apennines, Italy. Journal of Geophysical Research 106, 8811–8825.

Gmeindl, M., 1999. Sprödtektonische Strukturanalyse der Talhofstörung (Semmeringgebiet). Diploma Thesis, Institute of Applied Geology, University of Natural Resources and Life Sciences Vienna, 143 pp.

Hubbert, M.K., Rubey, W.W., 1959. Role of pore fluid pressure in the mechanics of overthrust faulting. Geological Society of America Bulletin 70, 115–205.

Janssen, C., Laube, N., Bau, M., Gray, D.R., 1998. Fluid regime in faulting deformation of the Waratah Fault Zone, Australia, as inferred from major and minor element analyses and stable isotope signatures. Tectonophysics 294, 109–130.

Katz, O., Reches, Z., Baer, G., 2003. Faults and their associated host rock deformation: part I. Structure of small faults in a quartz-syenite body, southern Israel. Journal of Structural Geology 25, 1675–1689.

Katz, Y., Weinberger, R., Aydin, A., 2004. Geometry and kinematic evolution of Riedel shear structures, Capitol Reef National Park, Utah. Journal of Structural Geology 26, 491–501.

Kennedy, L.A., Logan, J.M., 1998. Microstructures of cataclasites in a limestone-on-shale thrust fault: implications for low-temperature recrystallisation of calcite. Tectonophysics 295, 167–186.

Kennedy, L.A., White, J.C., 2001. Low-temperature recrystallization in calcite: mechanisms and consequences. Geology 29, 1027–1030.

Kerrich, R., 1986. Fluid infiltration into fault zones: chemical, isotopic and mechanical effects. Pure and Applied Geophysics 124, 225–267.

Kiechl, E., 2007. Die hydrogeologische Wirksamkeit von Störungen und Störungszonen am Beispiel der Talhofstörung (Ostalpen). Master thesis, Institut für Angewandte Geowissenschaften, Technische Universität Graz, 86 pp.

Kim, Y.-S., Peacock, D.C.P., Sanderson, D.J., 2004. Fault damage zones. Journal of Structural Geology 26, 503–507.

Kirschner, D.L., Kennedy, L.A., 2001. Limited sytectonic fluid flow in carbonate-hosted thrust faults of the Front Ranges, Canadian Rockies, inferred from stable isotope data and structures. Journal of Geophysical Research 106, 8827–8840.

Kurz, W., Wibberley, C.A.J., Imber, J., Holdsworth, R.E., Collettini, C., 2008. The internal structure of fault zones: fluid flow and mechanical properties – introduction. In: Geological Society of London Special Publication, vol. 99 1–3.

Linzer, H.-G., Decker, K., Peresson, H., DelÍMour, R., Frisch, W., 2002. Balancing lateral orogenic float of the Eastern Alps. Tectonophysics 354, 211–237.

Logan, J.M., Dengo, C.A., Higgs, N.G., Wang, Z.Z., 1992. Fabrics of experimental fault zones: their development and relationship to mechanical behaviour. In: Evans, B., Wong, T. (Eds.), Fault Mechanics and Transport Properties of Rocks. Academic Press, San Diego, pp. 33–67.

Logan, J.M., Friedman, M., Higgs, M., Dengo, C., Shimamoto, T., 1979. Experimental studies of simulated gouge and their application to studies of natural fault zones. Analysis of Actual Fault Zones in Bedrock, Conference Proceedings VIII, pp. 305–343.

Mandl, G., 1988. Mechanics of Tectonic Faulting. Models and Basic Concepts. Elsevier, Amsterdam, 407 pp.

Mandl, G., 2000. Faulting in Brittle Rocks. Springer, Berlin, 434 pp.

Mandl, G., 2005. Rock Joints – the Mechanical Genesis. Springer, Berlin, 221 pp.

Marquer, D., Burkhard, M., 1992. Fluid circulation, progressive deformation and mass-transfer processes in the upper crust: the example of basement–cover relationships in the External Crystalline Massifs, Switzerland. Journal of Structural Geology 14, 1047–1057.

Mazzoli, S., Zampetti, V., Zuppetta, A., 2001. Very low temperature, natural deformation of fine-grained limestone: a case study from the Lucania region, southern Apennines, Italy. Geodinamica Acta 14, 213–230.

Means, W.D., 1995. Shear zones and rock history. Tectonophysics 247, 157–160.

Micarelli, L., Benedicto, A., Invernizzi, C., Saint-Bezar, B., Michelot, J.L., Vergely, P., 2005. Influence of P/T conditions on the style of normal fault initiation and growth in limestones from the SE-Basin, France. Journal of Structural Geology 27, 1577–1598.

Micarelli, L., Benedicto, A., Wibberley, C.A.J., 2006. Structural evolution and permeability of normal fault zones in highly porous carbonate rocks. Journal of Structural Geology 28, 1214–1227.

Mollema, P.N., Antonellini, M., 1999. Development of strike-slip faults in the dolomites of the Sella Group, Northern Italy. Journal of Structural Geology 21, 273–292.

Naylor, M.A., Mandl, G., Seijpensteijn, C.H., 1986. Fault geometries in basement-induced wrench faulting under different initial stress states. Journal of Structural Geology 8, 737–752.

Olson, J.E., Pollard, D.D., 1991. The initiation and growth of en echelon veins. Journal of Structural Geology 13, 595–609.

Paterson, M.S., 1978. Experimental Rock Deformation – the Brittle Field. Springer, Berlin, 254 pp.

Peacock, D.C.P., Sanderson, D.J., 1992. Effects of layering and anisotropy on fault geometry. Journal of the Geological Society of London 149, 792–802.

Petit, J.-P., Wibberley, C.A.J., Ruiz, G., 1999. 'Crack-seal', slip: a new fault valve mechanism? Journal of Structural Geology 21, 1199–1207.

Pili, E., Poitrasson, F., Gratier, J.-P., 2002. Carbon–oxygen isotope and trace element constraints on how fluids percolate faulted limestones from the San Andreas Fault system: partitioning of fluid sources and pathways. Chemical Geology 190, 231–250.

Ramsay, J.G., 1980. The crack-seal mechanism of rock deformation. Nature 284, 135–139.

Ratschbacher, L., Frisch, W., Neubauer, F., Schmid, S.M., Neugebauer, J., 1989. Extension in compressional orogenic belts: the eastern Alps. Geology 17, 404–407.

Ratschbacher, L., Frisch, W., Linzer, H.-G., Merle, O., 1991. Lateral extrusion in the Eastern Alps. Part 2: structural analyses. Tectonics 10, 257–271.

Reches, Z., 1978. Analyses of faulting in three-dimensional strain field. Tectonophysics 47, 109–129.

Reches, Z., 1983. Faulting of rocks in three-dimensional strain fields; II: theoretical analyses. Tectonophysics 95, 133–156.

Reches, Z., Dietrich, J.H., 1983. Faulting of rocks in three-dimensional strain fields; I. Failured rocks in polyaxial, servo-control experiments. Tectonophysics 95, 111–132.

Reiter, F., Acs, P., 1996–2001. Tectonics FP 1.6.2, a 32-bit Windows™-Software for Structural Geology.

Riedel, W., 1929. Zur Mechanik geologischer Brucherscheinungen. Zentralblatt für Mineralogie. Geologie und Paläontologie 1929B, 354–368.

Rispoli, R., 1981. Stress fields about strike-slip faults inferred from stylolithes and tension gashes. Tectonophysics 75, T29–T39.

Sagy, A., Reches, Z., Roman, I., 2001. Dynamic fracturing: field and experimental observations. Journal of Structural Geology 23, 1223–1239.

Schmid, S.M., Fügenschuh, B., Kissling, E., Schuster, R., 2004. Tectonic map and overall architecture of the Alpine orogen. Eclogae geologicae Helvetiae 97, 93–117.

Schuster, R., Kurz, W., 2005. Eclogites in the Eastern Alps: high-pressure metamorphism in the context of Alpine orogeny. Mitteilungen der Österreichischen Mineralogischen Gesellschaft 150, 183–198.

Sibson, R.H., 1981. Controls on low-stress hydro-fracture dilatancy in thrust, wrench and normal fault terrains. Nature 289, 665–667.

Sibson, R.H., 1986. Brecciation processes in fault zones: inference from earthquake rupturing. Pure and Applied Geophysics 124, 159–175.

Sibson, R.H., 1990. Conditions for fault-valve behaviour. In: Knipe, R.J., Rutter, E.H. (Eds.), Deformation Mechanisms, Rheology and Tectonics. Geological Society of London Special Publication, vol. 54, pp. 15–28.

Sibson, R.H., 1992. Implications on fault-valve behaviour for rupture nucleation and recurrence. Tectonophysics 211, 283–293.

Sibson, R.H., 1996. Structural permeability of fluid-driven fault-fracture meshes. Journal of Structural Geology 18, 1031–1042.

Sibson, R.H., Moore, J.M., Rankin, A.H., 1975. Seismic pumping – a hydrothermal fluid transport mechanism. Journal of the Geological Society of London 131, 653–659.

Smith, S.A.F., Collettini, C., Holdsworth, R.E., 2008. Recognizing the seismic cycle along ancient faults: CO_2-induced fluidization of breccias in the footwall of a sealing low-angle normal fault. Journal of Structural Geology 30, 1034–1046.

Storti, F., Billi, A., Salvini, F., 2003. Particle size distributions in natural carbonate fault rocks: insights for non-self-similar cataclasis. Earth and Planetary Science Letters 206, 173–186.

Tarasewicz, J.P.T., Woodcock, N.H., Dickson, J.A.D., 2005. Carbonate dilation breccias: examples from the damage zone to the Dent Fault, northwest England. Geological Society of America Bulletin 117, 736–745.

Tchalenko, J.S., 1970. Similarities between shear zones of different magnitudes. Geological Society of America Bulletin 81, 1625–1640.

Tenthorey, E., Cox, S.F., Toff, H.F., 2003. Evolution of strength recovery and permeability during fluid–rock reaction in experimental fault zones. Earth and Planetary Science Letters 206, 161–172.

Vermilye, J.M., Scholz, C.H., 1998. The process zone: a microstructural view of fault growth. Journal of Geophysical Research 103, 12223–12237.

Wang, X., Neubauer, F., 1998. Orogen-parallel strike-slip faults bordering metamorphic core complexes: the Salzach-Enns fault zone in the Eastern Alps, Austria. Journal of Structural Geology 20, 799–818.

Wibberley, C.A.J., Shimamoto, T., 2003. Internal structure and permeability of major strike-slip fault zones: the Median Tectonic Line in Mie Prefecture, Southwest Japan. Journal of Structural Geology 25, 59–78.

Wibberley, C.A.J., Petit, J.-P., Rives, T., 2000. Micromechanics of shear rupture and the control of normal stress. Journal of Structural Geology 22, 411–427.

Wilcox, R.E., Harding, T.P., Seely, D.R., 1973. Basic wrench tectonics. American Association of Petroleum Geologists Bulletin 57, 74–96.

Willemse, E.J.M., Peacock, D.C.P., Aydin, A., 1997. Nucleation and growth of strike-slip faults in limestones from Somerset, U.K. Journal of Structural Geology 19, 1461–1477.

Woodcock, N.H., Dickson, J.A.D., Tarasewicz, J.P.T., 2007. Transient permeability and reseal hardening in fault zones: evidence from dilation breccia textures. In: Geological Society of London Special Publications, vol. 270 43–53.

Yasahuara, H., Marone, C., Elsworth, D., 2005. Fault zone restrengthening and frictional healing: the role of pressure solution. Journal of Geophysical Research 110 2004JB003327.